Anionic Doping in Layered Transition Metal Chalcogenides for Robust Lithium-Sulfur Batteries

Chen Huang, Jing Yu, Chao Yue Zhang, Zhibiao Cui, Ren He, Linlin Yang, Bingfei Nan, Canhuang Li, Junshan Li, Laura Simonelli, Oleg Usoltsev, Jordi Arbiol, Yao-Jie Lei, Qing Sun*, Guoxiu Wang * and Andreu Cabot**

C. Huang, J. Yu, C. Y. Zhang, R. He, L. L. Yang, B. F. Nan, C. H. Li, Q. Sun, A. Cabot
Catalonia Institute for Energy Research-IREC. Sant Adrià de Besòs, Barcelona 08930, Spain
E-mail: acabot@irec.cat; sunqing@hit.edu.cn

C. Huang
Department of Chemistry, University of Barcelona 08028, Spain

J. Yu, J. Arbiol
Catalan Institute of Nanoscience and Nanotechnology (ICN2), CSIC and BIST, Campus UAB, Bellaterra, 08193 Barcelona, Catalonia, Spain.

C. Y. Zhang
Key Laboratory for Magnetism and Magnetic Materials of the Ministry of Education & School of Physical Science & Technology; Lanzhou University Lanzhou 730000, China

Z. B. Cui
Shenzhen Key Laboratory of Special Functional Materials & Shenzhen Engineering Laboratory for Advance Technology of Ceramics, College of Materials Science and Engineering, Shenzhen University, Shenzhen 518060, P. R. China

J. S. Li
Institute for Advanced Study; Chengdu University 610106, Chengdu, China

L. Simonelli, O. Usoltsev
ALBA Synchrotron, 08290 Cerdanyola del Vallès, Barcelona, Catalonia, Spain

Y. J. Lei
Institute for Superconducting & Electronic Materials, Australian Institute of Innovative Materials, University of Wollongong, Innovation Campus, Squires Way, North Wollongong, NSW, 2500, Australia
E-mail: Yaojie.Lei@uts.edu.au

Y. J. Lei , G. X. Wang
Centre for Clean Energy Technology, School of Mathematical and Physical Sciences, Faculty of Science, University of Technology Sydney, Sydney, NSW, 2007, Australia
E-mail: guoxiu.wang@uts.edu.au

Q. Sun
Zhengzhou Research Institute, Harbin Institute of Technology, Zhengzhou 450000, China

J. Arbiol and A. Cabot
ICREA Pg. Lluis Companys, 08010 Barcelona, Catalonia, Spain

* *Corresponding authors*

Keywords: lithium-sulfur battery, induced lattice, Bi_2Se_3, Se vacancies, lithium polysulfides.

Abstract

Lithium-sulfur batteries (LSBs) are among the most promising next-generation energy storage technologies. However, slow Li-S reaction kinetics at the LSB cathode limit their energy and power densities. To address these challenges, this study introduces an anionic doped transition metal chalcogenide as an effective catalyst to accelerate the Li-S reaction. Specifically, a tellurium-doped, carbon-supported bismuth selenide with Se vacancies (Te-Bi_2Se_{3-x}@C) is presented as a sulfur host in LSB cathodes. X-ray absorption and *in-situ* X-ray diffraction analyses reveal that Te doping induces lattice distortions and modulates the local coordination environment and electronic structure of Bi atoms to promote the catalytic activity toward the conversion of polysulfides. Additionally, the generated Se vacancies alter the electronic structure around atomic defect sites, increase the carrier concentration, and activate unpaired cations to effectively trap polysulfides. As a result, LSBs based on Te-Bi_2Se_{3-x}@C/S cathodes demonstrate outstanding specific capacities of 1508 $mAh \cdot g^{-1}$ at 0.1C, excellent rate performance with 655 $mAh \cdot g^{-1}$ at 5C, and near-integral cycle stability over 1000 cycles. Furthermore, under high sulfur loading (6.4 $mg \cdot cm^{-2}$), a specific capacity of 1251 $mAh \cdot g^{-1}$ is sustained at 0.1C current rate, with 998.7 $mAh \cdot g^{-1}$ retained after 500 cycles under lean electrolyte conditions (6.8 $\mu L \cdot mg^{-1}$).

1. Introduction

Lithium-sulfur batteries (LSBs) have emerged as a promising alternative to Li-ion batteries, offering high energy density, specific capacity, and environmental benefits. However, the commercial viability of LSBs is significantly hindered by challenges associated with the sulfur cathode and lithium metal anode.[2] Key issues include the poor conductivity of sulfur (S_8) and its discharge product, Li_2S, which impede electronic and ionic transport during electrochemical reactions in the cathode. Additionally, severe volume expansion and the migration of lithium polysulfides (LiPSs) compromise long-term cycling stability.[2b, 3] The sluggish Li-S reaction kinetics further limit sulfur utilization and output power, especially under the high sulfur loadings and lean electrolyte conditions required for practical applications. On the anode side, lithium metal faces challenges such as uncontrolled dendrite growth and significant volume changes during repeated plating/stripping processes, leading to serious safety concerns and suboptimal cycle performance.[4]

To overcome the practical challenges faced by LSB cathodes, several strategies have been proposed, including the development of cathode sulfur hosts,[5] multifunctional separators,[6] and functional binders.[7] In the first direction, high surface area porous carbon materials are commonly utilized as sulfur hosts due to their affordability, excellent electrical conductivity, lightweight, and capability to physically confine polysulfides.[8] However, their non-polar nature results in a poor affinity for trapping polar polysulfides and facilitating their conversion.[9] To enhance the performance of carbon hosts, especially in activating the Li-S reaction and inhibiting polysulfide migration, the incorporation of transition metal compounds, especially layered transition metal cogenides (LTMCs), has shown considerable promise.[10] These materials provide stronger chemical interactions with polysulfides and excellent catalytic properties, significantly improving the electrochemical performance of LSBs. However, despite the typical nanosheet-like morphology of LTMCs, they expose a moderate number of active sites and they are characterized by slow charge transfer kinetics.[12] These challenges call for additional optimization of these materials, often through material doping, to fully harness their potential.

To enhance the catalytic efficiency of LTMCs, various strategies have been proposed[10-11,

[13] Among them, the introduction of vacancies, especially anionic vacancies, has emerged as a particularly effective approach.[3a, 9a, 14] Anionic vacancies not only inject additional free electrons within the LTMC lattice but also modify the coordination environment of the surrounding metal atoms, activating them to capture more polysulfides, and thus facilitating their conversion.[3a, 15] Additionally, anionic vacancies can distort the crystal lattice symmetry,[13c] shifting the charge center within the unit cell. This displacement generates a built-in electric field that facilitates charge transfer.[11a, 16] Thus the rational engineering of this lattice strain presents an additional promising strategy to modify the electronic structure of the LTMC, thereby enhancing its catalytic performance.

In this study, we engineer Te-doped Bi_2Se_3 supported on a nanostructured carbon polyhedral framework (Te-Bi_2Se_{3-x}@C). The incorporation of Te atoms is designed to induce lattice distortion and modify the local structure of the catalyst. Concurrently, the creation of Se vacancies adjusts the electronic structure around atomic defect sites and increases the number of charge carriers within the crystal. We evaluate the catalytic performance and LiPS affinity of this material for its potential use as a sulfur host in the cathode of Li-S batteries. Finally, LSB coin cells are assembled and tested to assess their performance and stability, including under conditions of high sulfur loading and lean electrolyte.

2. Results and Discussions

Te-Bi_2Se_{3-x}@C composites were produced through the annealing of Bi_2Se_3@C in a Te-rich atmosphere (see details in the Supporting Information, SI). Initially, Bi_2Se_3@C was synthesized by selenizing a Bi@C composite, which itself was derived from the carbonization of a Bi-based metal-organic framework (Bi-MOF) precursor under an argon atmosphere. The Bi-MOF was synthesized via a solvothermal reaction involving bismuth nitrate pentahydrate and trimesic acid in a solvent mixture of dimethylformamide (DMF) and methanol (CH_3OH), where each Bi^{3+} ion coordinated with six trimecic acid (H_3BTC) molecules.[17] The resulting Te-Bi_2Se_{3-x}@C composite was then combined with S to produce Te-Bi_2Se_{3-x}@C/S electrodes using a melt-infiltration process (**Figure 1a**).

The precursor Bi-MOF displayed a 1D rod-like morphology with a diameter of ca. 2 μm (**Figure S1a**). Upon calcination at 600 °C in an Ar atmosphere, the Bi-MOF was transformed

into carbon nanorods embedded with Bi@C nanoparticles (**Figure S1b**). These Bi@C nanorods and an excess of Se powder were annealed under the Ar atmosphere to produce Bi_2Se_3@C particles that preserved the rod-like architecture of the initial Bi@C (**Figure S1c**). With the addition of Te and the subsequent annealing step, rod-like structures containing a large dispersion of nanoparticles on their surface were obtained (**Figure S1d**).

Atomic resolution aberration-corrected (AC) high-angle annular dark field scanning transmission electron microscopy (HAADF STEM) images (**Figure 1b**) of Te-Bi_2Se_{3-x}@C showed the presence of Bi_2Se_3 (red and blue border area). These regions primarily consist of a five-layer sequence arranged in an A-B-A-B-A (Se-Bi-Se-Bi-Se) pattern (**Figure 1c**). Additionally, the presence of stacking faults is evidenced by the merging of the A-B-A-B-A-B-A sequence (Se-Bi-Se-Bi-Se-Bi-Se, yellow ellipse). The influence of Te on the Bi_2Se_3 lattice was assessed using HAADF STEM analysis of Bi_2Se_3@C (**Figure S2)**. The Bi_2Se_3 lattice in this sample exhibits no significant stacking faults, with only the Se-Bi-Se-Bi-Se sequence (orange area) visible. Therefore, the defects observed in the Te-Bi_2Se_{3-x}@C sample are likely due to the introduction of Te atoms into the Bi_2Se_3 lattice, which can disrupt the stacking sequence and induce faults during crystal growth. Besides, a subtle lattice distortion is observed in different directions in Te-Bi_2Se_{3-x}@C (**Figure 1d-e and S3**). This distortion is primarily attributed to three factors: 1) the Coulombic interaction localized around Te atoms; 2) Jahn-Teller distortion arising from the mismatch between Te and Se; and 3) differences in the atomic radius of Te and Se.

Energy dispersive x-ray spectroscopy (EDS) STEM analysis showed a homogenous distribution of Te, Se, and Bi on Te-Bi_2Se_{3-x}@C (**Figures 1f and S4,5**). Inductively coupled plasma mass spectrometry (ICP-MS) analysis yielded the atomic ratio of Te at 3.8 %, well below that of Bi (40.0 %) and Se (56.2 %) (**Table S1**). Moreover, we compared the iDPC and HAADF-STEM images obtained on the samples before (Bi_2Se_3@C) and after doping (Te-Bi_2Se_{3-x}@C) (**Figure 1g,h and S6**). Interestingly, in the doped sample (Te-Bi_2Se_{3-x}@C), some of the atomic columns corresponding to Se atoms showed a clear increase in intensity (both in HAADF and in iDPC STEM images), indicating a local replacement of Se atoms by Te. This effect is due to the fact that the iDPC STEM intensity is linearly proportional to Z, while the

HAADF STEM image intensity is barely proportional to Z^2. Since Te has an atomic number of 52, which is greater than that of Se (34) but less than that of Bi (83), it is reasonable to speculate that intensity profiles showing an increased intensity at the Se columns in both, iDPC STEM (**Figure 1g**) and HAADF STEM (**Figure 1h**) images, correspond to Te atoms occupying positions originally held by Se. We also observe that this Se-to-Te substitution predominantly occurs at the edges of the Se-Bi-Se-Bi-Se sequence, which is consistent with the lower interlayer binding energies, facilitating the accommodation of lattice distortions in these regions.

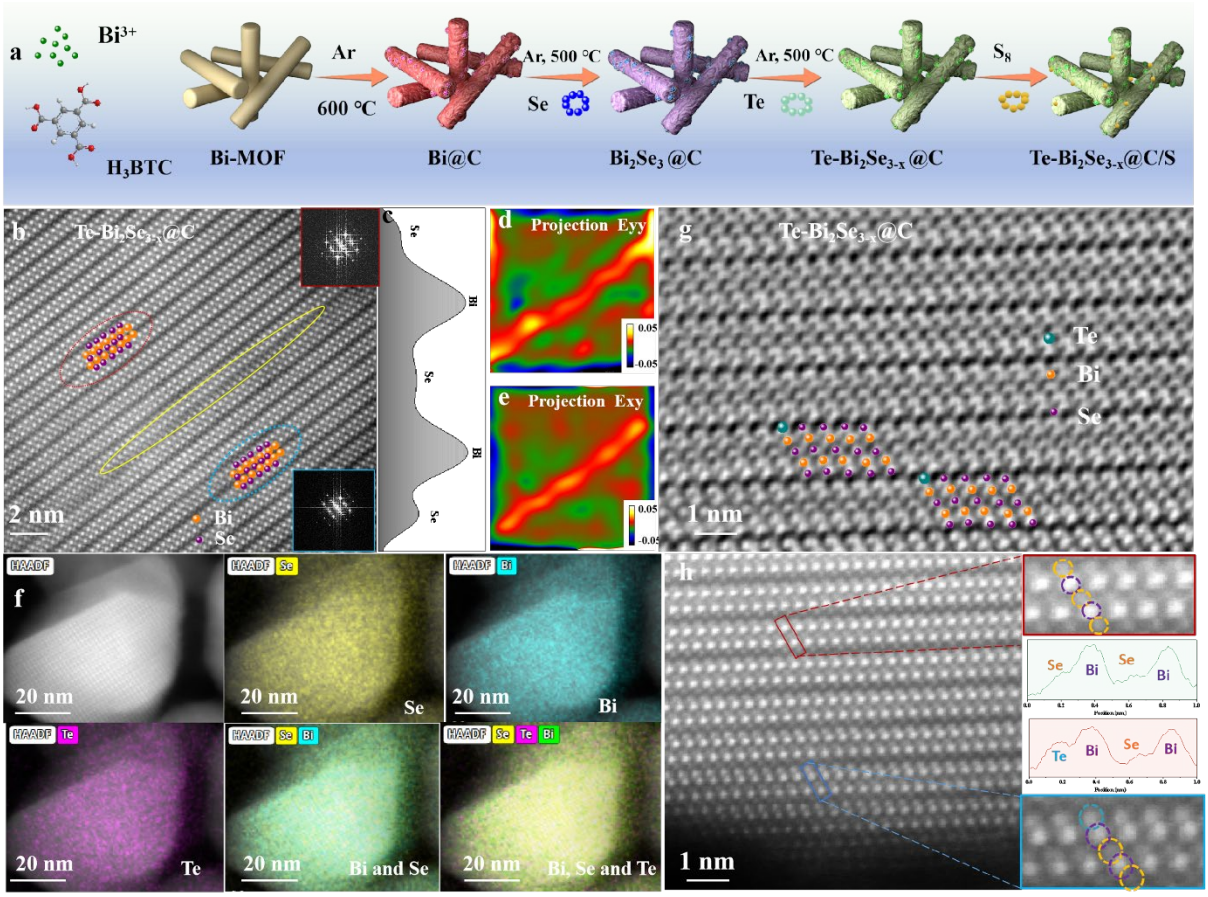

Figure 1. (a) Schematic diagram of the synthesis of the Te-Bi_2Se_{3-x}@C/S cathode material. (b) High-resolution AC HAADF-STEM image of Te-Bi_2Se_{3-x}@C. (c) Se-Bi-Se-Bi-Se pattern in Te-Bi_2Se_{3-x}@C. (d,e) Lattice distortion of Te-Bi_2Se_{3-x}@C in different directions (Eyy and Exy). (f) TEM-EDS spectra of a Te-Bi_2Se_{3-x}@C particle. (g) iDPC-STEM image of Te-Bi_2Se_{3-x}@C. (h) HAADF-STEM image of Te-Bi_2Se_{3-x}@C.

The XRD patterns of Te-Bi_2Se_{3-x}@C and Bi_2Se_3@C match well with the Bi_2S_3 phase, with no secondary phases (**Figure 2a**).[18] While Te doping does not change the crystal structure of

Bi_2Se_3@C, the XRD peaks of Te-Bi_2Se_{3-x}@C are slightly shifted to lower angles compared to Bi_2Se_3@C (**Figure S7**). This shift is primarily attributed to the larger radius of Te atoms compared to Se atoms, resulting in a larger lattice spacing for Te-Bi_2Se_{3-x}@C. Furthermore, with the introduction of Te atoms, the diffraction peak intensity of Te-Bi_2Se_{3-x}@C decreases, and a wider peak width is observed, indicating lower crystallinity. Overall, these results are consistent with the presence of Te within the Bi_2Se_3 lattice at Se sites.[19]

The electrode materials' specific surface area and pore volume were evaluated using N_2 adsorption/desorption isotherms. Specifically, the specific surface areas of Bi_2Se_3@C and Te-Bi_2Se_{3-x}@C were measured at 85.5 $m^2\ g^{-1}$ and 94.2 $m^2\ g^{-1}$, respectively (**Figure S8 and Table S2**). The pore diameters of the host materials predominantly fall within the range of 0-50 nm.

Electron paramagnetic resonance (EPR) was used to determine the presence of unpaired electrons associated with Se vacancies. As shown in **Figure S9a**, Te-Bi_2Se_{3-x}@C exhibits an obvious resonance signal at g=2.0.[3a, 20] In contrast, Bi_2Se_3@C exhibits no resonance signal under the same test conditions. This observation indicates that a notable density of Se vacancies was generated in Bi_2Se_3 upon Te doping.

The Raman spectra of Te-Bi_2Se_{3-x}@C and Bi_2Se_3@C are presented in **Figure S9b**. The peak at 130 cm^{-1} is associated with the E_{2g} mode of Bi_2Se_3.[15a, 21] In comparison with Bi_2Se_3@C, the Raman peak of Te-Bi_2Se_{3-x}@C shows a noticeable negative shift, aligning with the XRD results. To evaluate the degree of graphitization of the carbon, the intensities of the D band (at 1350 cm^{-1}) and the G band (at 1590 cm^{-1}) were compared. These Raman vibrational modes are associated with the disordered structure and bond stretching motion of sp^2 hybridized carbon, respectively (**Figure S9c**).[13d, 22] Defective carbon mainly provides more catalytic active sites for electrochemical reactions, while graphitized carbon enhances and accelerates charge transfer. Te-Bi_2Se_{3-x}@C exhibits a larger I_D/I_G ratio, indicating that the doping of Te increases the defects in the carbon materials.

The chemical composition and valence state of the elements within the two composites were analyzed using X-ray photoelectron spectroscopy (XPS). The Te atomic ratio within the Te-Bi_2Se_{3-x}@C sample calculated from the XPS spectra was Te/Bi/Se = 4/36/60 (**Table S3**), which matches well with ICP data, thus showing no major segregation of Te to the few surface-

most layers of the Te-Bi_2Se_{3-x} particles. The high-resolution Bi 4f XPS spectrum of Te-Bi_2Se_{3-x}@C was fitted with two doublets. A first doublet, at binding energies of 157.4 eV ($4f_{7/2}$) and 162.7 eV ($4f_{5/2}$), is associated with Bi^{3+} within the selenide lattice (**Figure 2b**). The second doublet, at 158.5 eV ($4f_{7/2}$) and 163.8 eV ($4f_{5/2}$) in Te-Bi_2Se_{3-x}@C is associated with Bi^{3+} in a more electronegative environment, possibly forming Bi_2O_3, $Bi_2(SeO_3)_3$, Bi_2SeO_2, or another oxidized form of Bi_2Se_3.[3h, 23] The same two doublets are also obtained for Bi_2Se_3/C but both are redshifted with respect to the Bi 4f XPS spectrum of Te-Bi_2Se_{3-x}@C. The high-resolution Se 3d XPS spectrum of Te-Bi_2Se_{3-x}@C (**Figure 2c**) displays three distinct doublets, corresponding to Se^{2-} in Bi_2Se_3 at 53.0 eV (Se $3d_{5/2}$),[3h, 24] Se^0 at 55.4 eV (Se $3d_{5/2}$), and SeOx (SeO_2, $Bi_2(SeO_3)_3$, Bi_2SeO_2) at 58.1 eV (Se $3d_{5/2}$).[25] The detection of elemental selenium indicates that not all of the elemental selenium, which was introduced in large excess during the second annealing step, fully participated in the formation of the selenide or was removed by evaporation.[26] The Se 3d XPS spectrum of Bi_2Se_3@C exhibits the same three doublets, though all are redshifted a similar value compared with Te-Bi_2Se_{3-x}@C. The consistent direction and magnitude of the binding energy shifts in both the Se 3d and Bi 4f XPS spectra suggest an upward shift of the Fermi level of Te-Bi_2Se_{3-x}@C relative to Bi_2Se_3@C, in agreement with the electronic donor role played by ionized selenium vacancies generated by the introduction of larger Te^{2-}ions at Se^{2-} sites.[3h, 13a] The C1s XPS spectra of Te-Bi_2Se_{3-x}@C and Bi_2Se_3@C present three characteristic peaks corresponding to C-C, C-O, and C=O at binding energies of 284.6 eV, 286.2 eV, and 288.6 eV, respectively (**Figure S10a**).[3a] The high-resolution Te 3d XPS spectrum of Te-Bi_2Se_{3-x}@C displays two doublets related to Te^{2-} within a metal chalcogenide at 574.2 eV (Te $3d_{5/2}$) and a Te-O chemical environment at 576.1 eV (Te $3d_{5/2}$) related to the air exposure of the material before XPS analysis (**Figure S10b**).[16] The ratio of oxidized Te is higher than that of oxidized Se. This is related to the electronic structure of Te playing a role in its higher oxidation tendency when exposed to air. Te has a lower ionization energy, making it easier for Te atoms to lose electrons and become oxidized, resulting in Te^+ or Te^{2+} states. In contrast, Se has a higher ionization energy, making it less prone to electron loss and therefore less likely to oxidize as extensively as Te. Besides, the preferential location of Te at the edges of the Se-Bi-Se-Bi-Se sequence, due to its larger size, can also promote its relative

enhanced oxidation upon air exposure.

The conductivity of Te-Bi_2Se_{3-x}@C samples (7.8×10^2 S cm^{-1}) was systematically higher than that of Bi_2Se_3@C (5.5×10^2 S cm^{-1}) across all pressure conditions, as measured by a four-probe method (**Figure S11a**). While the main contribution to electronic transport is primarily from carbon, this improved conductivity is attributed to the additional carriers introduced by the incorporation of Te.

The total density of states (TDOS) of Bi_2Se_3, calculated using density functional theory (DFT), reveals a band gap at the Fermi level, consistent with the semiconductor nature of the material (**Figure S11b**). In contrast, the electronic structure of Te-Bi_2Se_{3-x} shows the emergence of a distinct hybrid band within the conduction band, leading to a significant increase in TDOS at the Fermi level. This enhanced TDOS at the Fermi level is associated with improved charge transport properties, aligning with the experimentally observed increase in conductivity. It should be noted that the Te-Bi_2Se_{3-x} model included both Se vacancies and structural distortions generated when relaxing the model (see details in the SI).

The chemical state and coordination of Bi atoms were further investigated using X-ray absorption near-edge structure spectroscopy (XANES) and extended X-ray absorption fine structure spectroscopy (EXAFS). The white-line intensity of Te-Bi_2Se_{3-x}@C and Bi_2Se_3@C is higher than that of Bi foil, indicating their electronic states are at higher energy than the Bi (0) state in Bi foil. The absorption edges of Te-Bi_2Se_{3-x}@C and Bi_2Se_3@C are positioned between the absorption edges of the metallic Bi foil (Bi^0) and Bi_2O_3 (Bi^{3+}), indicating that Bi exhibits valence between 0 and +3 (**Figure 2d**).[27] Compared to Bi_2Se_3@C, Te-Bi_2Se_{3-x}@C exhibit a slight negative shift in the white line intensity, confirming that Bi in Te-Bi_2Se_{3-x}@C has a lower valence state compared to Bi_2Se_3@C[2b] (**inset Figure 2d**).

The Fourier-transformed k_3-weighted EXAFS spectra reveal a reduction in the intensity of the unique shell scattering peak (2.30 Å) corresponding to the Bi-Se bond in Te-Bi_2Se_{3-x}@C (**Figure 2e**). This reduction primarily stems from the presence of Se vacancies, leading to a decrease in the coordination number of Bi with Se.[13a] EXAFS curve fitting and the derived structural parameters (**Figure 2f-i and S12-13**) show the coordination number of Se and Bi centers in Bi_2Se_3@C (N=6.0) is significantly higher than in Te-Bi_2Se_{3-x}@C (N=4.6). This

observation suggests that Te atoms are substituting Se atoms within the structure. Additionally, the length of the Bi-Se bond in Te-Bi_2Se_{3-x}@C (2.81 Å) is slightly longer than in Bi_2Se_3@C (2.79 Å), a difference that can be attributed to the influence of Se vacancies.

Wavelet transform (WT) analysis (**Figure 2j-m**) was used to further unveil the structural disorder and charge redistribution around the Bi atoms. In Te-Bi_2Se_{3-x}@C, a slight shift towards a shorter radial distance is observed compared to Bi_2Se_3@C. This shift suggests that the alteration in bond length is primarily due to a weakening of Bi-Se coordination. These changes in the coordination environment affect the electron distribution at the surface, which is likely to influence the interaction with polysulfides and alter the kinetics of the catalyzed Li-S reaction.

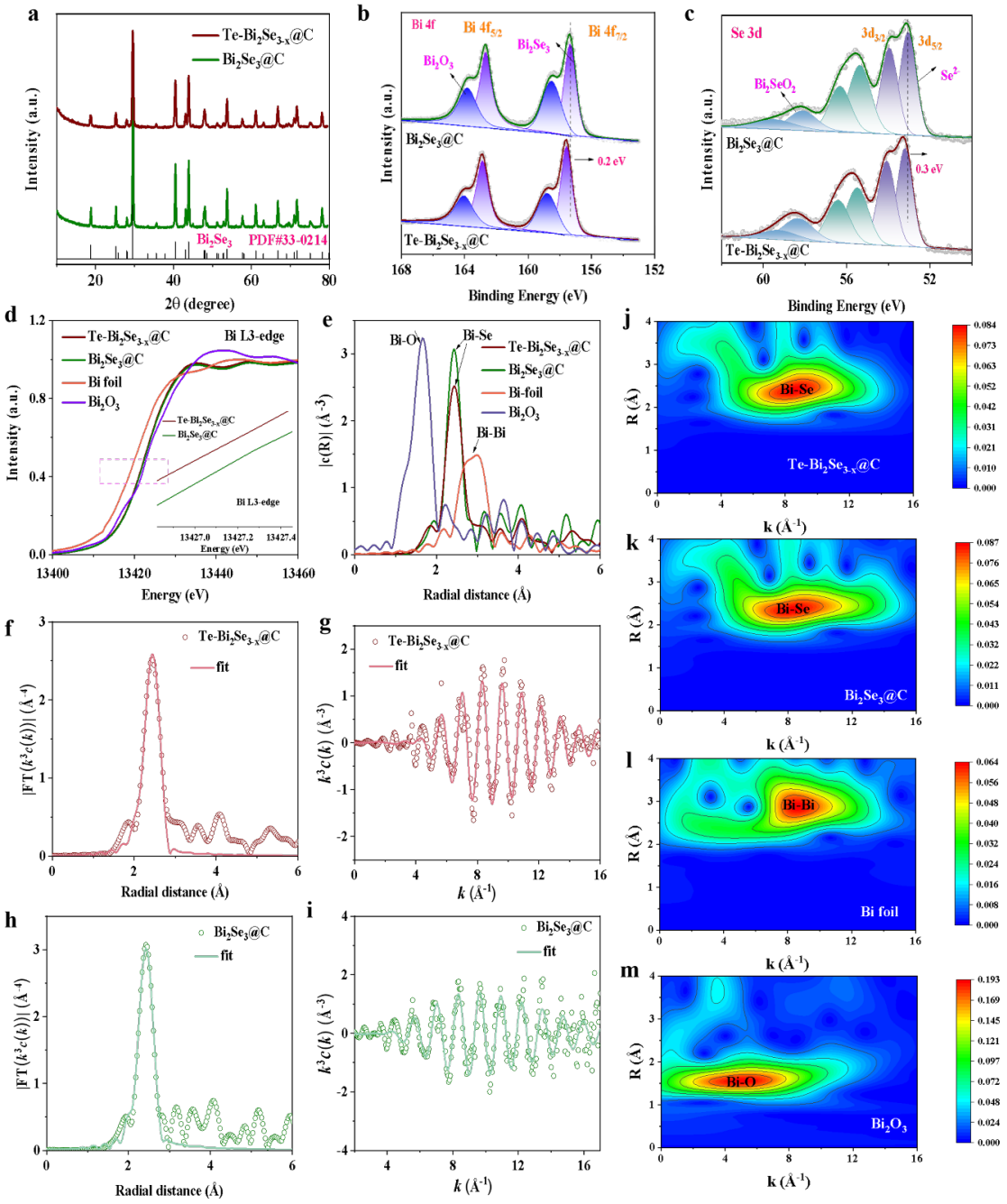

Figure 2. (a) XRD patterns of Te-Bi_2Se_{3-x}@C and Bi_2Se_3@C. (b,c) High-resolution Bi 4f (b) and Se 3d (c) XPS spectra of Te-Bi_2Se_{3-x}@C and Bi_2Se_3@C. (d) Bi L3-edge XANES of Te-Bi_2Se_{3-x}@C, Bi_2Se_3@C, Bi foil, and Bi_2O_3. (e) FT-EXAFS spectra of Te-Bi_2Se_{3-x}@C, Bi_2Se_3@C, Bi foil, and Bi_2O_3. (f) FT-EXAFS fitting curves of Bi L3-edge for Te-Bi_2Se_{3-x}@C at R space. (g) FT-EXAFS fitting curves of Bi L3-edge for Te-Bi_2Se_{3-x}@C at k_3 space. (h) FT-EXAFS fitting curves of Bi L3-edge for Bi_2Se_3@C at R space. (i) FT-EXAFS fitting curves of Bi L3-edge for Bi_2Se_3@C at k_3 space. (j-m) WT contour plots for Te-Bi_2Se_{3-x}@C (j), Bi_2Se_3@C

(k), Bi foil (l), and Bi_2O_3 (m).

To assess the LiPS adsorption capacity of the host materials, they were immersed in a 0.5 mM Li_2S_6 solution overnight. After this period, the Li_2S_6 solution containing only porous carbon (Super P) largely retained its original orange-brown color, while the solution with Bi_2Se_3@C showed a slight lightening (inset **Figure 3a**). In contrast, the color of the Li_2S_6 solution containing Te-Bi_2Se_{3-x}@C almost completely vanished, indicating nearly complete adsorption of Li_2S_6 by the Te-Bi_2Se_{3-x}@C host material. This observation was further confirmed using UV-vis absorption spectroscopy (**Figure 3a**).

XPS analysis of the material after the LiPS adsorption test (Te-Bi_2Se_{3-x}@C-Li_2S_6) revealed a significant bluedshift in both the Bi 4f, Se 3d and Te 3d orbitals compared to the fresh sample (Te-Bi_2Se_{3-x}), suggesting a strong interaction between the sample and the Li_2S_6 **(Figure 3b,c and S14)**.[3a, 5b]

DFT calculations were conducted to evaluate the theoretical adsorption capacity of the host materials for polysulfides. **Figures S15-18** present the adsorption models for the various host materials interacting with polysulfides. As noted above, the theoretical calculation model accounted for the effect of vacancies and lattice distortions induced by doping, which are automatically considered during the geometry optimization process. Compared to Bi_2Se_3, Te-Bi_2Se_{3-x} exhibits a higher adsorption capacity for LiPSs. Specifically, the adsorption energies of Bi_2Se_3 and Te-Bi_2Se_{3-x} for Li_2S_4 are -1.98 eV and -2.81 eV, respectively (**Figure 3d**).

In-situ XRD was used to characterize the evolution of S_8 and Li_2S during the charge/discharge of a cell (see details in the SI, **Figure 3e-g**). During the discharge stage, a notable delay is observed in the weakening of the Bragg signal intensity for the α-S_8 phase in the Bi_2Se_3@C/S and Super P/S electrodes compared to the Te-Bi_2Se_{3-x}@C/S electrode. The characteristic Bragg signal of the α-S_8 phase persists throughout the discharge process, indicating a relatively slower reaction kinetics within the Bi_2Se_3@C and Super P electrodes compared to Te-Bi_2Se_{3-x}@C. As lithiation progresses, in the fully discharged state, the relative intensity of the Li_2S signal in the Bi_2Se_3@C/S and Super P/S cathodes is significantly lower than that in the Te-Bi_2Se_{3-x}@C/S. This suggests insufficient polysulfide conversion during lithiation in the former (Bi_2Se_3@C/S and Super P/S), with the α-S_8 phase failing to fully lithiate,

consistent with the persistent presence of characteristic signals throughout the characterization process. Upon full charge, during delithiation, all electrodes exhibit characteristic signals corresponding to β-S_8. However, the β-S_8 signal intensity in the Bi_2Se_3@C/S and Super P/S is weak, and a small Bragg signal corresponding to the α-S_8 phase remains from the initial stage. In contrast, the Te-Bi_2Se_{3-x}@C electrode shows negligible α-S_8 phase signal and a strong β-S_8 XRD, suggesting full conversion of S_8 during the charge/discharge cycle.

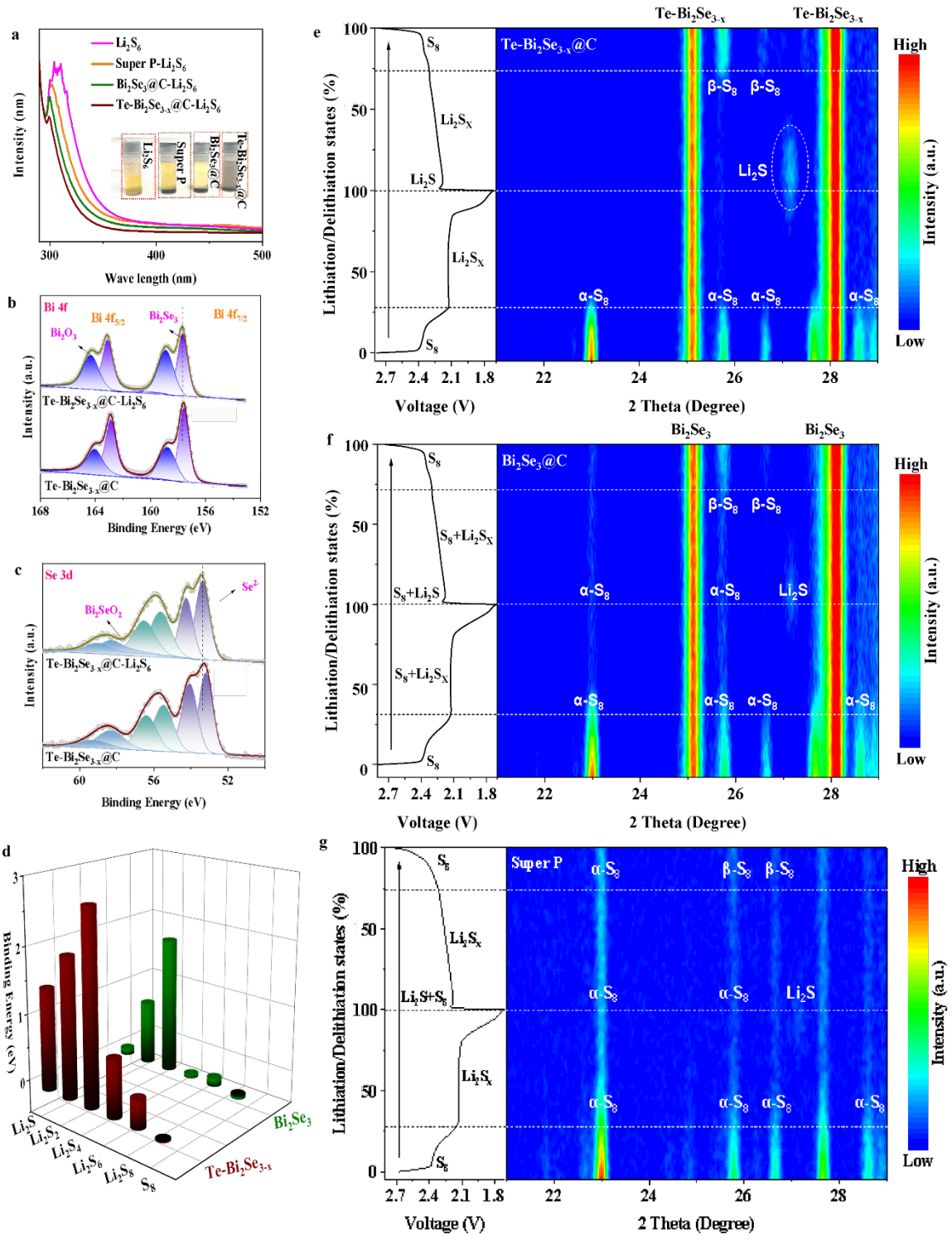

Figure 3. (a) UV-vis absorption spectra and photographs (inset) of Li_2S_6 solutions containing different materials after overnight adsorption. (b,c) High-resolution Bi 4f and Se 3d XPS spectra of Te-Bi_2Se_{3-x}@C before and after Li_2S_6 adsorption. (d) DFT-calculated adsorption energies of Te-Bi_2Se_{3-x}@C and Bi_2Se_{3-x}@C with different polysulfides (S_8, Li_2S_8, Li_2S_6, Li_2S_4, Li_2S_2, and

Li_2S). (e-g) *In situ* XRD patterns during charging and discharging of cells based on Te-Bi_2Se_{3-x}@C/S, Bi_2Se_3@C/S, and Super P/S cathodes.

To assess the catalytic performance of the host materials, 2032 coin-type symmetric cells were assembled using the host materials in both electrodes These cells were tested without sulfur, utilizing an electrolyte containing Li_2S_6 (see details in the SI). The cyclic voltammetry (CV) curves of the Te-Bi_2Se_{3-x}@C-based symmetric cells exhibited the highest peak current densities compared to those of Bi_2Se_3@C and Super P (**Figure 4a**). This result suggests that Te doping effectively enhances the LiPS conversion kinetics. Additionally, the CV curves of Te-Bi_2Se_{3-x}@C in a Li_2S_6-free electrolyte showed purely capacitive behavior, confirming that the capacity contribution observed in the Li_2S_6-containing electrolyte is indeed due to the conversion of polysulfides. Linear sweep voltammetry (LSV) further demonstrated that the Te-Bi_2Se_{3-x}@C electrode exhibited the lowest overpotentials and the lowest Tafel slopes for both the reduction and oxidation of S within polysulfides (**Figures 4b,c and S19**). This result corroborates that the introduction of Te into Bi_2Se_3 significantly accelerates the polysulfide conversion kinetics. Additionally, electrochemical impedance spectroscopy (EIS) analyses of the symmetric cells revealed that the Te-Bi_2Se_{3-x}@C electrodes had the lowest charge transfer resistance (10.5 Ω), further suggesting enhanced charge transfer kinetics during the sulfur redox reaction due to the introduction of Te (**Figure S20**)

The analysis of the Li_2S nucleation step on Te-Bi_2Se_{3-x}@C, Bi_2Se_3@C, and Super P revealed that the Te-Bi_2Se_{3-x}@C cathode exhibited the highest current response during the 2.05 V potential static test (**Figure 4d-f**). According to Faraday's law (Q=It, where Q is the capacity, I is the discharge current, and t is the time), the calculated capacity of Te-Bi_2Se_{3-x}@C was 229 mAh g^{-1}, well above that of Bi_2Se_3@C (188 mAh g^{-1}) and Super P (133 mAh g^{-1}). This indicates that the Te-Bi_2Se_{3-x}@C cathode has a superior ability to facilitate Li_2S nucleation, contributing to its enhanced electrochemical performance.

The breaking of the S-S bond of the polysulfides adsorbed on the different surfaces was investigated using DFT calculations (**Figure 4g, h and S21**). The analysis revealed significant alterations in electron density within bonding and antibonding states near the Fermi level upon polysulfide adsorption onto the host materials. In comparison to Bi_2Se_3, the TDOS of Te-Bi_2Se_{3-}

$_x$ exhibits an upward shift, resulting in a lower stability of the S-S bond. Consequently, Te-Bi_2Se_{3-x} facilitates the cleavage of S-S bonds, thereby enhancing the kinetics of the Li-S reaction.

During the reduction of sulfur, S_8 initially reacts with two Li^+ to generate Li_2S_8, which is subsequently converted into Li_2S_6, Li_2S_4, Li_2S_2, and ultimately into Li_2S. DFT calculations of the Gibbs free energy for the entire reaction process on the surface of Te-Bi_2Se_{3-x} and Bi_2Se_3 (**Figure 4i**) revealed that the energy barrier for the rate-determining step (Li_2S_4 to Li_2S_2) on the Te-Bi_2Se_{3-x} surface (0.18 eV) was significantly lower than that on the Bi_2Se_3 surface (0.46 eV). This reduced energy barrier on the Te-Bi_2Se_{3-x} surface is consistent with the experimental results showing Te-Bi_2Se_{3-x} to promote the entire Li-S reaction process.

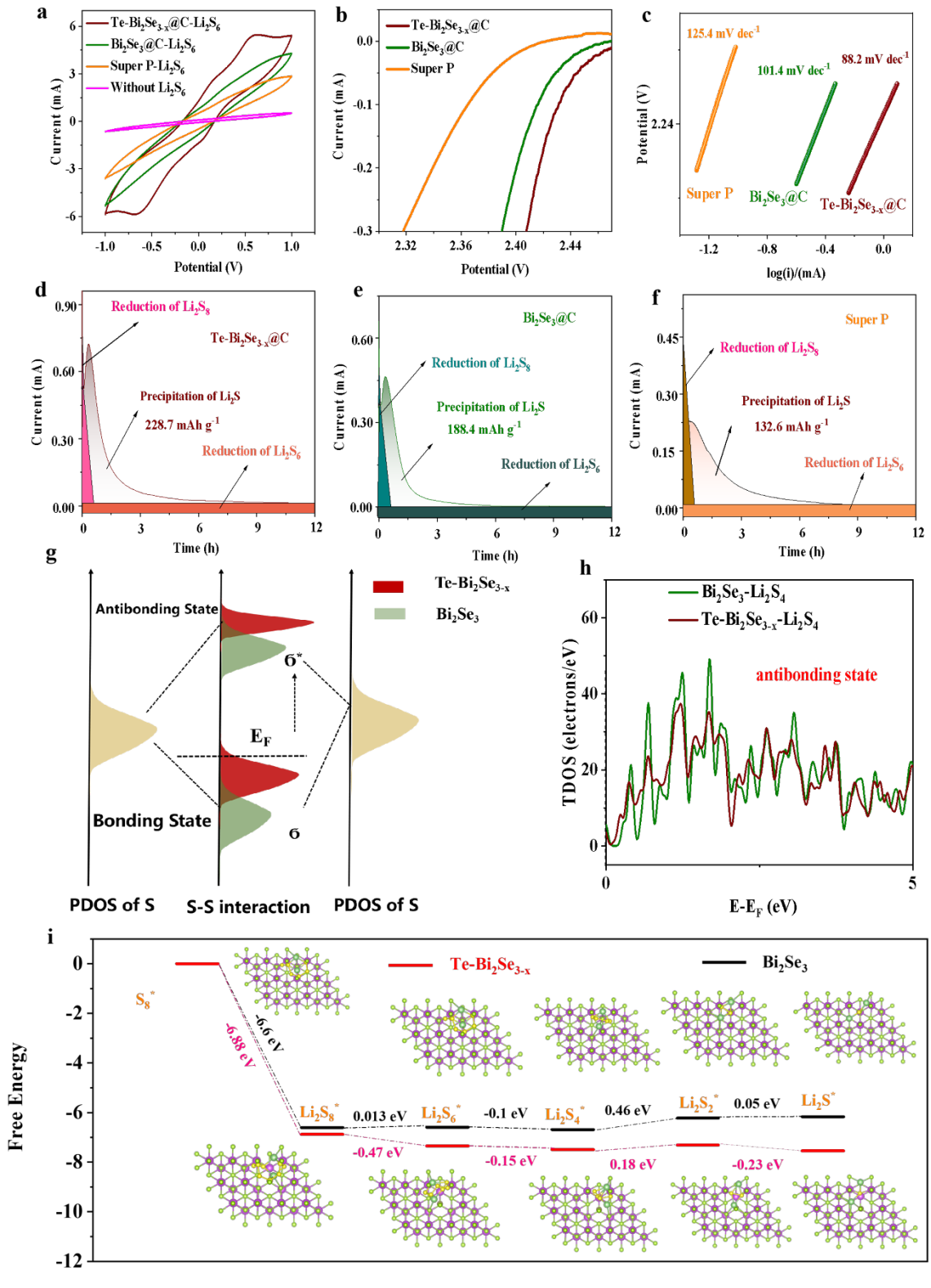

Figure 4 (a) CV curves of symmetric cells based on Te-Bi_2Se_{3-x}@C, Bi_2Se_3@C, and Super P electrodes at a scan rate of 5 mV s^{-1}. (b,c) Tafel curves of the different electrodes within the symmetric cells. (d-f) Li_2S deposition curves of Te-Bi_2Se_{3-x}@C (d), Bi_2Se_3@C (e), and Super P (f) at 2.05V constant voltage. (g) Energy level diagram illustrating orbital hybridization for

the S-S bond is depicted below. The Fermi level of the substrate (E_F) is indicated, with σ and σ* denoting bonding and antibonding states, respectively. (h) TDOS curves for Bi_2Se_3 and Te-Bi_2Se_{3-x} after adsorption of Li_2S_4. (i) Gibbs free curves and model optimization structure of Te-Bi_2Se_{3-x} and Bi_2Se_3.

To evaluate the electrochemical performance of the host materials within LSB cells, the materials were infiltrated with S (see details in the SI). XRD analysis confirmed the presence of sulfur in the final electrode material (**Figure S22**). Besides, thermogravimetric analysis (TGA) quantified the sulfur content in Te-Bi_2Se_{3-x}@C/S, Bi_2Se_{3-x}@C/S, and Super P/S as 69.5%, 68.3%, and 66.8%, respectively (**Figure S23**). Coin cells were assembled using the sulfur composite electrode as the cathode, lithium foil as the anode, and a solution composed of 1.0 M lithium bis(trifluoromethanesulfonyl) imide and 2% $LiNO_3$ in a mixture of 1,3-dioxolane (DOL) and 1,2-dimethoxyethane (DME) in a 1:1 volume ratio as electrolyte. The galvanostatic charge/discharge (GCD) curves of the cells at a 0.1C current rate are shown in **Figure 5a**. Two distinct plateaus emerged during the discharge process. The first discharge plateau, with a capacity denoted as Q1, was attributed to the conversion of S_8 to long-chain polysulfides (S_8 into Li_2S_4). The second discharge plateau, with a capacity Q2, accounted for the solid-solid reaction of polysulfides gaining electrons and reducing to insoluble Li_2S_2, and eventually to Li_2S.[2a, 23] The unique charging voltage plateau is associated with the complete conversion of polysulfides back to S_8. Consistent with previous results, the Te-Bi_2Se_{3-x}@C/S cathode demonstrated the highest initial specific capacity (1508 mAh g^{-1}), outperforming Bi_2Se_3@C/S (1274 mAh g^{-1}) and Super P/S (1078 mAh g^{-1}) (**Table S4**). **Figure S24** illustrates the charging and discharging mechanism of LSBs.

We also observed the polarization potential ΔE (**Figure 5b**), defined as the difference between the oxidation platform and the second reduction platform of the Li-S reaction,[3g, 28] was significantly lower for Te-Bi_2Se_{3-x}@C/S (109 mV) compared to Bi_2Se_3@C/S (166 mV) and Super P/S (186 mV). Additionally, the Q_2/Q_1 ratio was used to quantify the catalytic activity of the host material toward LiPS conversion (**Figure 5b**).[25a, 29] The first plateau involves 4 electrons, while the second plateau involves 12 electrons, leading to a theoretical Q_2/Q_1 ratio of 3 for a complete 16-electron S_8 lithiation process. However, this ratio is typically lower than

3 due to the dissolution of polysulfides that cannot further participate in the reaction and the incomplete reduction from Li_2S_4 to Li_2S during the second discharge. The closer the Q_2/Q_1 ratio is to 3, the stronger the conversion ability of the host material to convert polysulfides.[3a] Experimentally, the Q_2/Q_1 ratio measured for Te-Bi_2Se_{3-x}@C/S (2.74) was significantly higher than that of Bi_2Se_3@C/S (2.57) and Super P/S (2.43), demonstrating that the Te-doped host material has excellent catalytic ability to accelerate the conversion of polysulfides.

The galvanostatic charge/discharge (GCD) curves of Te-Bi_2Se_{3-x}@C/S, Bi_2Se_3@C/S, and Super P/S at different current rates and the rate performance of the cells are displayed in **Figures 5c-e and S25**. At current densities of 0.1C, 0.2C, 0.5C, 1C, 2C, 3C, and 5C, the specific capacity for Te-Bi_2Se_{3-x}@C/S was 1508, 1262, 1033, 923, 815, 756, and 655 mAh g^{-1}, respectively. These values are significantly higher than those obtained for the two reference electrodes. Even at the highest current rate tested (5C), a clear voltage plateau can be observed for Te-Bi_2Se_{3-x}@C/S, indicating a fast conversion of polysulfides in this electrode. Upon returning to a 0.2C current rate, the specific capacity of the Te-Bi_2Se_{3-x}@C/S electrode reached 1134 mAh g^{-1}, demonstrating notable reversibility.

The CV curves of different electrodes at a scan rate of 0.1 mV s^{-1} within a potential window from 1.7 V to 2.8 V are depicted in **Figures 5f and S26**. The Te-Bi_2Se_{3-x}@C/S-based cell exhibits distinct dual reduction peaks, corresponding to the conversion of S_8 to Li_2S_X ($4 \leq X \leq 8$) and insoluble Li_2S_2/Li_2S, respectively. The oxidation peak is attributed to the conversion between polysulfides and S_8.[30] When compared with other cathodes (Bi_2Se_3@C/S and Super P/S), Te-Bi_2Se_{3-x}@C/S demonstrates the highest current response and the lowest peak-separation polarization, again consistent with the superior catalytic activity of this material.

The diffusion coefficient of Li^+ was qualitatively evaluated through CV tests at scan rates ranging from 0.1 mV s^{-1} to 0.4 mV s^{-1}. The current of the redox peak displays a linear relationship with the square root of the scan rate (**Figure S27**). Consequently, the diffusion coefficient of Li^+ (D_{Li}) was calculated using the Randles-Sevcik equation.[11b, 14, 31]

$$I_p = 2.69 \times 10^5 \, n^{1.5} A \, D_{Li}^{0.5} C_{Li} \, v^{0.5}$$

where n is the number of charges, A is the geometric area of the electrode, and C_{Li} represents the concentration of Li^+. D_{Li} was obtained from a linear fitting of I_p vs. $v^{0.5}$ (**Figure 5g**)

Compared with Bi_2Se_3@C/S and Super P/S, Te-Bi_2Se_{3-x}@C/S exhibits the steepest slope, i.e. the highest D_{Li} as obtained from the anodic peak and the two cathodic peaks, at 6.4×10^{-7} cm^2 s^{-1}, 3.4×10^{-7} cm^2 s^{-1} and 4.2×10^{-7} cm^2 s^{-1}, respectively. These values are significantly higher than those obtained for the other two cathodes.

The electrocatalytic activity of the different sulfur hosts was further analyzed by measuring the onset potential at a current density of 10 μA cm^{-2} above the baseline current (**Figures 5h and S28**).[5a, 30b] Compared to Bi_2Se_3@C/S and Super P/S, Te-Bi_2Se_{3-x}@C/S exhibited the lowest anodic peak onset potential and the highest cathodic peak onset potential, indicating superior redox kinetics.

As shown in **Figures 5i and S29**, the EIS spectrum of Te-Bi_2Se_{3-x}@C/S revealed the smallest semicircle in the high-frequency region, corresponding to the lowest charge transfer resistance (R_{ct}) at 38.6 Ω, compared to Bi_2Se_3@C/S (79.6 Ω) and Super P/S (97.5 Ω).[13d, 22b] Additionally, the Te-Bi_2Se_{3-x}@C/S cathode displayed a lower Warburg resistance in the low-frequency region, indicating faster diffusion of Li^+ ions.[32] Furthermore, the cycled Te-Bi_2Se_{3-x}@C/S electrode exhibited a smaller diffusion resistance compared to the fresh electrode, which is attributed to the chemical activation of the cathode, involving the dissolution and redistribution of the active species.[2a]

The galvanostatic intermittent titration technique (GITT) was employed to examine how the composite layer affects the dynamic changes in internal resistance during the cell discharge-charge cycle. GITT measurements were performed at a 0.1C current density. The voltage measured after the resting period was identified as the open-circuit voltage (V_{OC}), whereas the voltage recorded during the current pulse was denoted as the short-circuit voltage (V_{SC}). As illustrated in **Figures 5j-k and S30**, the Te-Bi_2Se_{3-x}@C/S cell shows a smaller voltage difference between V_{OC} and V_{SC} compared to the Bi_2Se_3@C/S and Super P/S. Using this data, the dynamic internal resistance (ΔiR) was calculated with the following equation.

$$\Delta iR = |V_{OC} - V_{SC}|/I$$

Throughout the entire charge-discharge cycle, ΔiR of the Te-Bi_2Se_{3-x}@C/S cell remains significantly below that of Bi_2Se_3@C/S and Super P/S cells, which is consistent with the enhanced charge transport and reaction kinetics attributed to Te doping (**Figure 5l**)

To evaluate the cycling stability, repeated GCD tests were conducted at a 0.1C current rate (**Figures 5m and S31**). After 300 cycles, the Te-Bi_2Se_{3-x}@C/S cathode demonstrated the highest capacity retention (94.6 %), significantly outperforming Bi_2Se_3@C/S (76.2 %) and Super P/S (54.2 %). At a higher current rate of 1C, Te-Bi_2Se_{3-x}@C/S maintained a capacity retention rate of 91.4 % after 1000 cycles, whereas cells with Bi_2Se_3@C/S and Super P/S cathodes failed after approximately 500 cycles (**Figure 5n**). The performance of the Te-Bi_2Se_{3-x}@C/S electrode was also compared with that of previously reported cathodes (**Figure S32 and Table S5**). At a current density of 0.1C, Te-Bi_2Se_{3-x}@C/S exhibited the highest specific capacity, underscoring its exceptional performance among state-of-the-art cathode materials.[2a, 3b, 13c, 15c, 33]

After 100 cycles at a 1C current rate, the cells were dismantled, and their separators were examined. Notably, the separator from the Te-Bi_2Se_{3-x}@C/S cell was the most translucent compared to those from Bi_2Se_3@C/S and Super P/S cells, indicating minimal penetration of LiPSs into the membrane (**Figure S33**). Additionally, analysis of the recovered Li anode from the Te-Bi_2Se_{3-x}@C/S cell revealed a lower sulfur concentration, further confirming the effective suppression of LiPS diffusion and indicating better stability and protection of the Li anode (**Figure S34**).

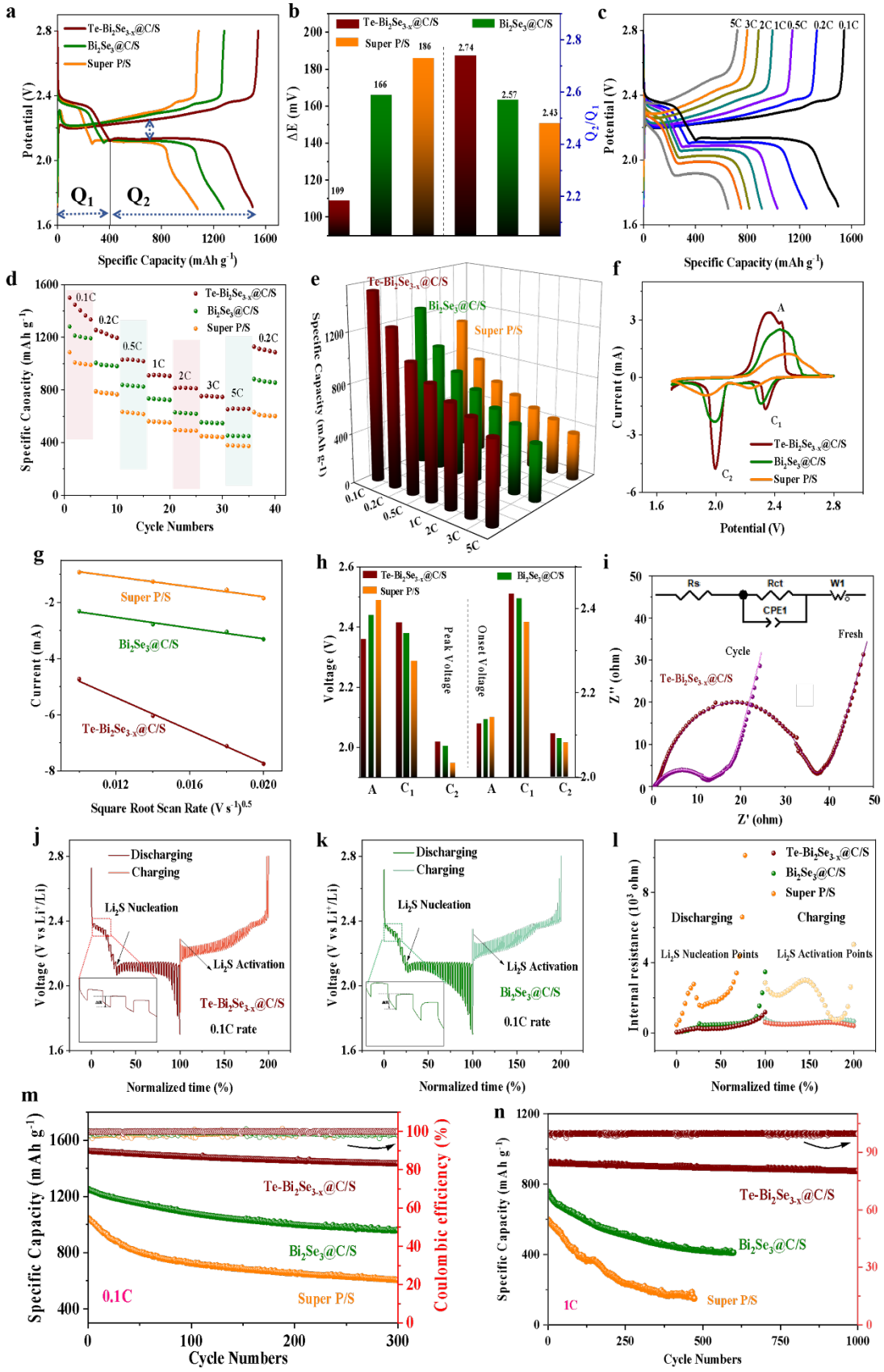

Figure 5. (a) GCD curves of different electrodes at a current rate of 0.1C. (b) Polarization voltage and Q_2/Q_1 ratio for Te-Bi_2Se_{3-x}@C/S, Bi_2Se_3@C/S, and Super P/S. (c) GCD curve of

Te-Bi_2Se_{3-x} in the voltage window 1.7-2.8 V and current densities from 0.1C to 5C. (d,e). Rate performance of different cathodes. (f) CV curves within a voltage window of 1.7-2.8V at a scan rate of 0.1mV s^{-1}. (g) Peak current vs. the square root of the rate. (h) Peak and onset potentials of Te-Bi_2Se_{3-x}@C/S, Bi_2Se_3@C/S, and Super P/S. (i) EIS spectra of Te-Bi_2Se_{3-x}@C/S before and after 100 cycles. The inset displays the equivalent circuit used to fit the data. (j,k) GITT curves on Te-Bi_2Se_{3-x}@C/S (j) and Bi_2Se_3@C/S (k). (l) Internal resistances vs. normalized discharge-charge time. (m) Cycling stability at a current density of 0.1C. (n) Cycling stability at a current rate of 1C.

To gain insight into the role of Bi in the charge and discharge process of Te-Bi_2Se_{3-x}@C, the Bi-L3 XANES spectra were examined ex-situ during the discharging and charging of the battery. The XANES spectra at four points during the battery discharging from 2.3 V to 1.7 V are displayed in **Figure 6**. As the discharge progresses, the position of the white line peak of the Bi-L3 edge shifts significantly to a higher energy (**Figure 6a**). This shift indicates that Bi gradually loses electrons, increasing the valence state of Bi. This observation suggests a strong interaction between the Bi atoms in the host material and the S atoms in the polysulfide. During the discharge process, Bi transfers electrons to S and LiPSs, promoting the reduction reaction of S or LiPSs. Conversely, during the charging process, the Bi L3 edge shifts to a lower energy level, indicating that Bi transitions to a lower valence state (**Figure 6b**). Thus, during charging, Li_2S/Li_2S_2/Li_2S_4 transfer electrons to Bi, thereby accelerating the oxidation reaction. These results indicate that Bi can serve as an effective electron reservoir to catalyze the redox reaction of S during both discharge and charge through electron transfer.

Additionally, the EXAFS results for Te-Bi_2Se_{3-x}@C/S during the charge and discharge process indicate that the average bond length of the first shells of Bi-Se is 2.3 Å (**Figure 6c,d**). This suggests that the Te-Bi_2Se_{3-x}@C phase remains stable without undergoing any phase transitions throughout the charge and discharge cycles. As illustrated in **Figure 6e-f**, the WT of the Te-Bi_2Se_{3-x}@C/S electrode demonstrates that the maximum values at all charge and discharge voltages are concentrated around 7.5 Å. There is no significant energy shift, confirming that Te-Bi_2Se_{3-x}@C remains in a stable state as a catalyst throughout the charge and discharge process.

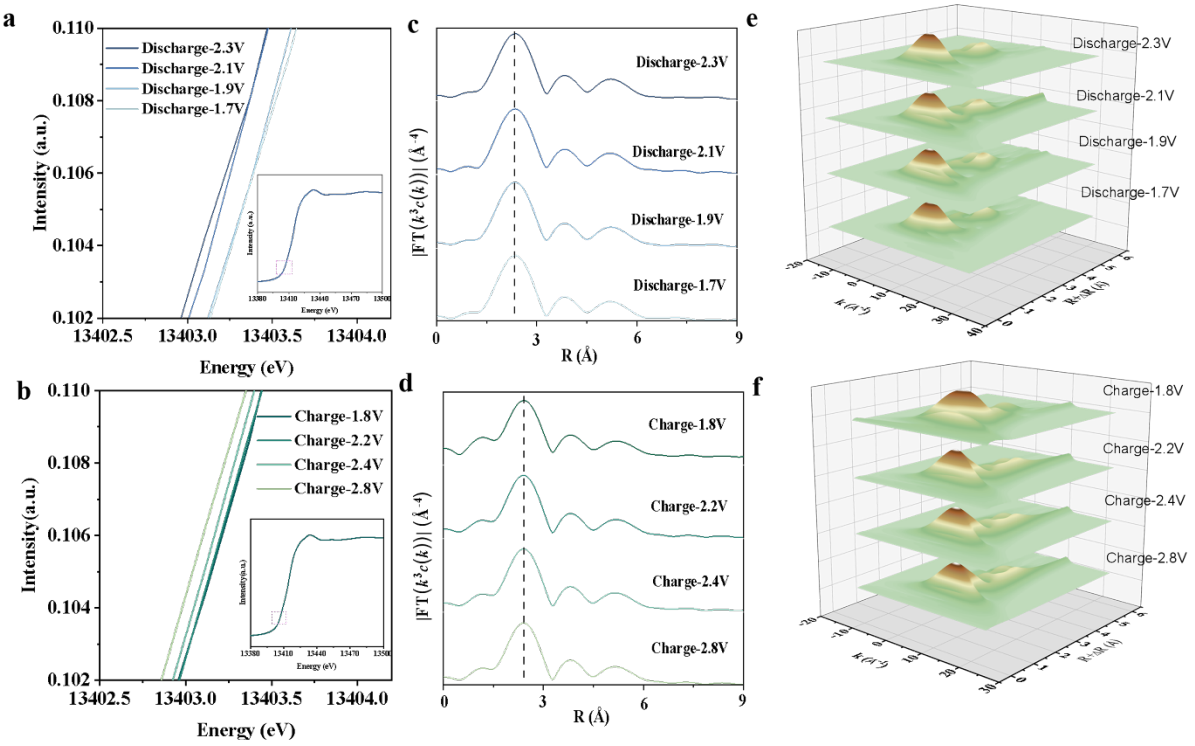

Figure 6. (a,b) Enlargements of the shift of the Bi L3-edge from ex situ XANES spectra of the Te-Bi_2Se_{3-x}@C/S sample during the discharge (a) and the charge (b) processes. Insets show the full XANES spectra. (c,d) k3-weighted FT-EXAFS curves of Te-Bi_2Se_{3-x}@C/S in R space during discharge and charge processes. (e,f) WT plots of the Bi L3-edge of the Te-Bi_2Se_{3-x}@C/S sample during discharge (e) and charge processes (f).

The loading amount of active material (S) and the amount of electrolyte used are critical parameters for evaluating the practical application of electrode materials. To assess applicability, Te-Bi_2Se_{3-x}@C/S-based cells with a high sulfur loading of 6.4 $mg \cdot cm^{-2}$ were assembled. The GCD curves and rate performance of one such high sulfur loading cell are presented in **Figure 7a,b**. At current densities of 0.1C, 0.2C, 0.5C, 1C, 2C, and 3C, the specific capacities were 1248, 1032, 932, 830, 755, and 632 $mAh \cdot g^{-1}$, respectively. This corresponds to areal capacities of 8.0, 6.6, 6.0, 5.3, 4.8, and 4.0 $mAh \cdot g^{-1}$, all of which exceed the typical values obtained in cathode materials for Li-ion batteries. The cycling stability of the high sulfur loading Te-Bi_2Se_{3-x}@C/S-based cell was further tested under different electrolyte contents. With electrolyte amounts of 10.4 $\mu L \cdot mg^{-1}$ and 6.8 $\mu L \cdot mg^{-1}$, the capacity retention after 300 cycles at a 0.1C current rate was 92.8% and 90.5%, respectively (**Figure 7c**). To further validate the practical application of Te-Bi_2Se_{3-x}@C/S cathodes, pouch-type batteries were assembled

using the Te-Bi_2Se_{3-x}@C/S cathode. In the pouch cell, the cathode exhibited an initial specific capacity of 1224 $mAh \cdot g^{-1}$ at a current density of 0.1C, retaining 86.7% of its capacity after 200 cycles (**Figure S35**). Additionally, **Figure 7d** demonstrates that two Te-Bi_2Se_{3-x}@C/S pouch cells connected in series were capable of powering an LED strip for over 30 min, showcasing the practical potential of this material in real-world applications.

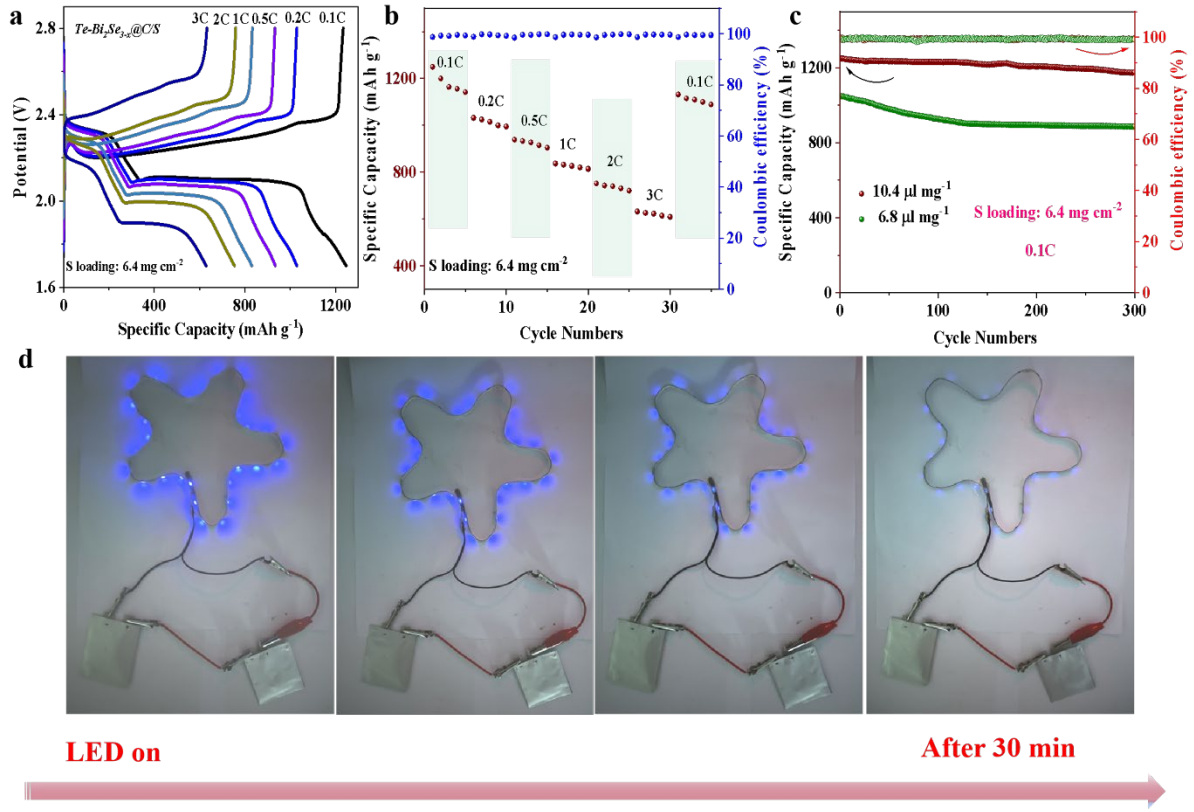

Figure 7. (a) GCD curves of Te-Bi_2Se_{3-x}@C/S cells with a high S loading (6.4 mg cm^{-2}). (b) Rate performance of the high S loading cell. (c) Cycling stability of Te-Bi_2Se_{3-x}@C/S at a current density of 0.1C under different electrolyte contents. (d) Te-Bi_2Se_{3-x}@C/S based pouch cells powering an LED strip.

3. Conclusion

In summary, both experimental results and theoretical calculations confirmed the effectiveness of ionic doping in Bi_2Se_3 for enhancing the performance of LSBs. Specifically, in Te-doped Bi_2Se_3, Te occupies the Se sits. Due to its larger atomic size, it generates Se vacancies, which leads to an increased concentration of free carriers in the electrode material. Additionally, the

increase of unpaired Bi cations provided additional active sites for LiPS adsorption and catalytic reactions, thereby promoting sulfur conversion kinetics. Simultaneously, Te doping induces lattice distortion within the Bi_2Se_3 material, causing a shift in the positive/negative charge center of the unit cell toward the negative direction. This phenomenon generates an intrinsic electric field, facilitating the transfer of charges within the cathode material. By leveraging doping, defects, and lattice distortion engineering, the Te-Bi_2Se_{3-x}@C cathode exhibited outstanding electrochemical performance, including high specific capacity (up to 1508 $mAh \cdot g^{-1}$ at 0.1C), excellent rate capability, and prolonged cycle stability, even under high sulfur loading and lean electrolyte conditions. Overall, this work offers valuable insights into the strategic design of ionically doped layered metal chalcogenide catalysts that enhance both polysulfide adsorption and redox activity in sulfur cathodes for advanced LSBs.

Supporting information

Supporting information is available from the author.

Acknowledgements

This work was financially supported by the 2BoSS project of the ERA-MIN3 program with the Spanish grant number PCI2022-132985 /AEI /10.13039 /501100011033, Generalitat de Catalunya 2021SGR01581 and 2021SGR00457 and European Union Next Generation EU / PRTR. C. H., J. Y. et.al thank the China Scholarship Council for the scholarship support. ICN2 is supported by the Severo Ochoa program from Spanish MCIN / AEI (Grant No.: CEX2021-001214-S). IREC and ICN2 are both funded by the CERCA Program/Generalitat de Catalunya. The authors thank the support from the project NANOGEN (PID2020-116093RB-C43), funded by MCIN/ AEI/10.13039/501100011033/ and by "ERDF A way of making Europe", by the "European Union". J. Li is grateful for the project supported by the Natural Science Foundation of Sichuan (2022NSFSC1229). This work has received funding from the "Spanish Ministry of Science and Innovation" through "Severo Ochoa" (CEX2019-000917-S) and "OXISOT" (PID2021-128410OB-I00). This study is part of the Advanced Materials program and was supported by MCIN with funding from the European Union Next Generation EU (PRTR-C17.I1) and by Generalitat de Catalunya. Part of the present work has been performed in the framework of Universitat Autònoma de Barcelona Materials Science PhD program. The authors

acknowledge the use of instrumentation as well as the technical advice provided by the Joint Electron Microscopy Center at ALBA (JEMCA). ICN2 acknowledges funding from Grant IU16-014206 (METCAM-FIB) funded by the European Union through the European Regional Development Fund (ERDF), with the support of the Ministry of Research and Universities, Generalitat de Catalunya. ICN2 is a founding member of e-DREAM.[34]

Conflict of Interest

The authors declare no conflict of interest.

Data Availability Statement

The data that support the findings of this study are available from the corresponding author upon reasonable request.

Reference

[1] a) B. Liu, R. Fang, D. Xie, W. Zhang, H. Huang, Y. Xia, X. Wang, X. Xia, J. Tu, *Energy environ. mater.* **2018**, 1, 196; b) L. Ren, J. Liu, Y. Zhao, Y. Wang, X. Lu, M. Zhou, G. Zhang, W. Liu, H. Xu, X. Sun, *Adv. Funct. Mater.* **2023**, 33, 2210509; c) X. Sun, Y. Qiu, B. Jiang, Z. Chen, C. Zhao, H. Zhou, L. Yang, L. Fan, Y. Zhang, N. Zhang, *Nat. Commun.* **2023**, 14, 291; d) J. Yu, C. Huang, O. Usoltsev, A. P. Black, K. Gupta, M. C. Spadaro, I. Pinto-Huguet, M. Botifoll, C. Li, J. Herrero-Martín, J. Zhou, A. Ponrouch, R. Zhao, L. Balcells, C. Y. Zhang, A. Cabot, J. Arbiol, *ACS Nano* **2024**, DOI: 10.1021/acsnano.4c05278.

[2] a) D. Fang, G. Wang, S. Huang, T. Chen Li, J. Yu, D. Xiong, D. Yan, X. Liang Li, J. Zhang, Y. Von Lim, S. A. Yang, H. Ying Yang, *Chem. Eng. J.* **2021**, 411, 128546; b) C. Huang, J. Yu, C. Y. Zhang, Z. Cui, J. Chen, W.-H. Lai, Y.-J. Lei, B. Nan, X. Lu, R. He, L. Gong, J. Li, C. Li, X. Qi, Q. Xue, J. Y. Zhou, X. Qi, L. Balcells, J. Arbiol, A. Cabot, *Adv. Mater.* **2024**, 36, 2400810; c) C. Li, J. Yu, C. Zhang, D. Yang, J. Wang, H. Li, C. Huang, K. Xiao, Y. Cheng, Y. Ren, X. Qi, T. Yang, J. Li, J. Wang, G. Henkelman, J. Arbiol, J. Nan, A. Cabot, *J. Colloid Interface Sci.* **2024**, 670, 61.

[3] a) C. Huang, J. Yu, C. Li, Z. Cui, C. Zhang, C. Zhang, B. Nan, J. Li, J. Arbiol, A. Cabot, *Adv. Funct. Mater.* **2023**, n/a, 2305624; b) H.-J. Li, K. Xi, W. Wang, S. Liu, G.-R. Li, X.-P. Gao, *Energy Stor. Mater.* **2022**, 45, 1229; c) D. Wang, F. Li, R. Lian, J. Xu, D. Kan, Y. Liu, G. Chen, Y. Gogotsi, Y. Wei, *ACS Nano* **2019**, 13, 11078; d) S. Li, W. Zhang, J. Zheng, M. Lv, H. Song, L. Du, *Adv. Energy Mater.* **2021**, 11, 2000779; e) J. He, A. Manthiram, *Adv. Energy Mater.* **2020**, 10, 2002654; f) D. Liu, C. Zhang, G. Zhou, W. Lv, G. Ling, L. Zhi, Q.-H. Yang, *Adv. Sci.* **2018**, 5, 1700270; g) X. Zhang, T. Yang, Y. Zhang, X. Wang, J. Wang, Y. Li, A. Yu, X. Wang, Z. Chen, *Adv. Mater.* **2023**, 35, 2208470; h) M. Li, D. Yang, J. J. Biendicho, X. Han, C. Zhang, K. Liu, J. Diao, J. Li, J. Wang, M. Heggen, R. E. Dunin-Borkowski, J. Wang, G. Henkelman, J. R. Morante, J. Arbiol, S.-L. Chou, A. Cabot, *Adv. Funct. Mater.* **2022**, 32, 2200529; i) C. Huang, J. Yu, C. Li, Z. Cui, C. Zhang, C. Zhang, B. Nan, J. Li, J. Arbiol, A. Cabot, *Adv. Funct. Mater.* **2023**, 33, 2305624; j) C. Li, D. Yang, J. Yu, J. Wang, C. Zhang, T. Yang, C. Huang, B. Nan, J. Li, J. Arbiol, Y. Zhou, Q. Zhang, A. Cabot, *Adv. Energy Mater.* **2024**, n/a, 2303551.

[4] B. Hu, J. Xu, Z. Fan, C. Xu, S. Han, J. Zhang, L. Ma, B. Ding, Z. Zhuang, Q. Kang, X. Zhang, *Adv. Energy Mater.* **2023**, 13, 2203540.

[5] a) W. Yao, W. Zheng, J. Xu, C. Tian, K. Han, W. Sun, S. Xiao, *ACS Nano* **2021**, 15, 7114; b) W. Liu, C.

Luo, S. Zhang, B. Zhang, J. Ma, X. Wang, W. Liu, Z. Li, Q.-H. Yang, W. Lv, *ACS Nano* **2021**, 15, 7491; c) C. Y. Zhang, X. Lu, X. Han, J. Yu, C. Zhang, C. Huang, L. Balcells, A. G. Manjón, J. Jacas Biendicho, J. Li, J. Arbiol, G. Sun, J. Y. Zhou, A. Cabot, *J. Am. Chem. Soc.* **2023**, 145, 18992.

[6] a) Y. Gong, Y. Wang, Z. Fang, S. Zhao, Y.-s. He, W. Zhang, J. Mu, L. Zhang, Z.-F. Ma, *Chem. Eng. J.* **2022**, 446, 136943; b) Y. Li, T. Gao, D. Ni, Y. Zhou, M. Yousaf, Z. Guo, J. Zhou, P. Zhou, Q. Wang, S. Guo, *Adv. Mater.* **2022**, 34, 2107638; c) Y.-H. Liu, L.-X. Li, A.-Y. Wen, F.-F. Cao, H. Ye, *Energy Stor. Mater.* **2023**, 55, 652.

[7] a) Q. Qi, X. Lv, W. Lv, Q.-H. Yang, *J. Energy Chem.* **2019**, 39, 88; b) M. J. Lacey, F. Jeschull, K. Edström, D. Brandell, *J. Power Sources* **2014**, 264, 8.

[8] a) M. Zheng, Y. Chi, Q. Hu, H. Tang, X. Jiang, L. Zhang, S. Zhang, H. Pang, Q. Xu, *J. Mater. Chem. A* **2019**, 7, 17204; b) R. Fang, K. Chen, L. Yin, Z. Sun, F. Li, H.-M. Cheng, *Adv. Mater.* **2019**, 31, 1800863; c) Y. Xie, J. Ao, L. Zhang, Y. Shao, H. Zhang, S. Cheng, X. Wang, *Chem. Eng. J.* **2023**, 451, 139017.

[9] a) Y. Zhang, C. Ma, C. Zhang, L. Ma, S. Zhang, Q. Huang, C. Liang, L. Chen, L. Zhou, W. Wei, *Chem. Eng. J.* **2023**, 452, 139410; b) J. Pu, W. Gong, Z. Shen, L. Wang, Y. Yao, G. Hong, *Adv. Sci.* **2022**, 9, 2104375; c) J. Mou, Y. Li, L. Ou, J. Huang, *Energy Stor. Mater.* **2022**, 52, 111.

[10] S. Hu, M. Yi, H. Wu, T. Wang, X. Ma, X. Liu, J. Zhang, *Adv. Funct. Mater.* **2022**, 32, 2111084.

[11] a) K. Zhang, G. Zhang, J. Qu, H. Liu, *Small* **2020**, 16, 1907001; b) M. J. Theibault, C. Chandler, I. Dabo, H. D. Abruña, *ACS Catal.* **2023**, 13, 3684.

[12] a) C. Tan, Z. Luo, A. Chaturvedi, Y. Cai, Y. Du, Y. Gong, Y. Huang, Z. Lai, X. Zhang, L. Zheng, X. Qi, M. H. Goh, J. Wang, S. Han, X.-J. Wu, L. Gu, C. Kloc, H. Zhang, *Adv. Mater.* **2018**, 30, 1705509; b) X. Yu, Y. Ding, J. Sun, *Iscience* **2023**.

[13] a) W. Yao, C. Tian, C. Yang, J. Xu, Y. Meng, I. Manke, N. Chen, Z. Wu, L. Zhan, Y. Wang, R. Chen, *Adv. Mater.* **2022**, 34, 2106370; b) W. Hou, P. Feng, X. Guo, Z. Wang, Z. Bai, Y. Bai, G. Wang, K. Sun, *Adv. Mater.* **2022**, 34, 2202222; c) H.-J. Li, Y.-H. Song, K. Xi, W. Wang, S. Liu, G.-R. Li, X.-P. Gao, *J. Mater. Chem. A* **2021**, 9, 10704; d) C. Huang, A. Gao, F. Yi, Y. Wang, D. Shu, Y. Liang, Z. Zhu, J. Ling, J. Hao, *Chem. Eng. J.* **2021**, 419, 129643; e) Z. Luo, D. Shu, F. Yi, J. Ling, M. Wang, C. Huang, A. Gao, *New J. Chem.* **2021**, 45, 22748.

[14] M. Yang, P. Liu, Z. Qu, F. Sun, Y. Tian, X. Ye, X. Wang, X. Liu, H. Li, *Nano Energy* **2022**, 104, 107922.

[15] a) K. Zou, X. Chen, W. Jing, X. Dai, P. Wang, Y. Liu, R. Qiao, M. Shi, Y. Chen, J. Sun, Y. Liu, *Energy Stor. Mater.* **2022**, 48, 133; b) X. Dai, X. Wang, G. Lv, Z. Wu, Y. Liu, J. Sun, Y. Liu, Y. Chen, *Small* **2023**, n/a, 2302267; c) H. Song, T. Li, T. He, Z. Wang, D. Fang, Y. Wang, X. L. Li, D. Zhang, J. Hu, S. Huang, *Chem. Eng. J.* **2022**, 450, 138115; d) Z. Ye, Y. Jiang, L. Li, F. Wu, R. Chen, *Adv. Mater.* **2022**, 34, 2109552; e) Y. Song, H. Li, J. Li, J. An, J.-J. Shao, G. Zhou, *J. Energy Chem.* **2023**, 87,51-60.

[16] B. Wang, L. Wang, D. Ding, Y. Zhai, F. Wang, Z. Jing, X. Yang, Y. Kong, Y. Qian, L. Xu, *Adv. Mater.* **2022**, 34, 2204403.

[17] Y. Liang, N. Song, Z. Zhang, W. Chen, J. Feng, B. Xi, S. Xiong, *Adv. Mater.* **2022**, 34, 2202673.

[18] a) R. He, S. Ou, Y. Liu, Y. Liu, D. Xu, *Chinese J. Catal.* **2022**, 43, 370; b) W. Liang, B. Chen, W. Lin, L. Shao, X. Shi, Z. Sun, *Mater. Lett.* **2023**, 332, 133542.

[19] Y. Liao, R. He, W. Pan, Y. Li, Y. Wang, J. Li, Y. Li, *Chem. Eng. J.* **2023**, 464, 142669.

[20] X. Ma, Y. Li, X. Long, H.-c. Luo, C. Xu, G. Wang, W. Zhao, *J. Energy Chem.* **2023**, 77, 227.

[21] J. H. Moon, H. Seong, G. Kim, Y. Jin, W. Nam, H. Yoo, T. Jung, K. Lee, M. Yang, S. Y. Cho, J. Choi, *Appl. Surf. Sci.* **2023**, 638, 157976.

[22] a) C. Huang, A. Gao, Z. Zhu, F. Yi, M. Wang, J. Hao, H. Cheng, J. Ling, D. Shu, *Electrochim. Acta* **2022**, 406, 139872; b) C. Huang, S. Lv, A. Gao, J. Ling, F. Yi, J. Hao, M. Wang, Z. Luo, D. Shu, *Chem. Eng. J.*

2022, 431, 134083.

[23] J. Li, L. Kang, K. Luo, Y. Huang, S. Zhong, D. Yan, *Ceram. Int.* **2023**, 49, 2613.

[24] a) G.-E. Lee, I.-H. Kim, Y. S. Lim, W.-S. Seo, B.-J. Choi, C.-W. Hwang, *J Korean Phys Soc* **2014**, 65, 696; b) P. H. Le, K. H. Wu, C. W. Luo, J. Leu, *Thin Solid Films* **2013**, 534, 659.

[25] a) X. Zhao, C. Zhang, G. Yang, Y. Wu, Q. Fu, H. Zhao, Y. Lei, *Inorg. Chem. Front.* **2021**, 8, 4267; b) Z. Li, H. Pan, W. Wei, A. Dong, K. Zhang, H. Lv, X. He, *Ceram. Int.* **2019**, 45, 11861; c) T. Yang, J. Liu, D. Yang, Q. Mao, J. Zhong, Y. Yuan, X. Li, X. Zheng, Z. Ji, H. Liu, G. Wang, R. Zheng, *ACS Appl. Energy Mater.* **2020**, 3, 11073; d) D. Khalafallah, W. Huang, M. Wunn, M. Zhi, Z. Hong, *J Energy Storage* **2022**, 45, 103716.

[26] Y.-C. Yeh, P.-H. Ho, C.-Y. Wen, G.-J. Shu, R. Sankar, F.-C. Chou, C.-W. Chen, *The Journal of Physical Chemistry C* **2016**, 120, 3314.

[27] S. Hu, X. Huang, L. Zhang, G. Li, S. Chen, J. Zhang, X. Liu, *Adv. Funct. Mater.* **2023**, 33, 2214161.

[28] C. Dong, C. Zhou, M. Wu, Y. Yu, K. Yu, K. Yan, C. Shen, J. Gu, M. Yan, C. Sun, L. Mai, X. Xu, *Adv. Energy Mater.* **2023**, 13, 2301505.

[29] D. Yang, C. Zhang, J. J. Biendicho, X. Han, Z. Liang, R. Du, M. Li, J. Li, J. Arbiol, J. Llorca, Y. Zhou, J. R. Morante, A. Cabot, *ACS Nano* **2020**, 14, 15492.

[30] a) C. Zhang, J. J. Biendicho, T. Zhang, R. Du, J. Li, X. Yang, J. Arbiol, Y. Zhou, J. R. Morante, A. Cabot, *Adv. Funct. Mater.* **2019**, 29, 1903842; b) D. Yang, M. Li, X. Zheng, X. Han, C. Zhang, J. Jacas Biendicho, J. Llorca, J. Wang, H. Hao, J. Li, G. Henkelman, J. Arbiol, J. R. Morante, D. Mitlin, S. Chou, A. Cabot, *ACS Nano* **2022**, 16, 11102.

[31] E. Ghasemiestahbanati, A. Shehzad, K. Konstas, C. J. Setter, L. A. O'Dell, M. Shaibani, M. Majumder, M. R. Hill, *J. Mater. Chem. A* **2022**, 10, 902.

[32] R. Chu, T. T. Nguyen, Y. Bai, N. H. Kim, J. H. Lee, *Adv. Energy Mater.* **2022**, 12, 2102805.

[33] a) S. Xin, T. Liu, J. Li, H. Cui, Y. Liu, K. Liu, Y. Yang, M. Wang, *Small* **2023**, 19, 2207924; b) H. Wu, H. Jiang, Y. Yang, C. Hou, H. Zhao, R. Xiao, H. Wang, *J. Mater. Chem. A* **2020**, 8, 14498.

[34] R. Ciancio, R. E. Dunin-Borkowski, E. Snoeck, M. Kociak, R. Holmestad, J. Verbeeck, A. I. Kirkland, G. Kothleitner, J. Arbiol, *Microscopy and Microanalysis* **2022**, 28, 2900.